Research Square

Preprints are preliminary reports that have not undergone peer review.
They should not be considered conclusive, used to inform clinical practice,
or referenced by the media as validated information.

Climatology of Large-Scale Atmospheric Conditions Favorable to Clear-Air Turbulence over Europe (1950–2025): The Role of Quasi-Biennial Solar Modulation

Gabriel Pascual
Universitat Politècnica de Catalunya: Universitat Politecnica de Catalunya
Julia Soliva
Universitat Politècnica de Catalunya: Universitat Politecnica de Catalunya
Jordi Mazon
jordi.mazon@upc.edu
Universitat Politècnica de Catalunya: Universitat Politecnica de Catalunya https://orcid.org/0000-0001-5527-3274
David Pino
Universitat Politècnica de Catalunya: Universitat Politecnica de Catalunya

Research Article

Keywords: Clear-air turbulence, ERA5 reanalysis, Synoptic-scale dynamics, Upper troposphere, Quasi-biennial solar modulation, Euro-Mediterranean region

Posted Date: June 26th, 2026

DOI: https://doi.org/10.21203/rs.3.rs-9844323/v1

License: This work is licensed under a Creative Commons Attribution 4.0 International License.
Read Full License

Version of Record: A version of this preprint was published at Climate Dynamics on October 9th, 2026. See the published version at https://doi.org/10.1007/s00382-026-08418-3.

Climatology of Large-Scale Atmospheric Conditions Favorable to Clear-Air Turbulence over Europe (1950–2025): The Role of Quasi-Biennial Solar Modulation

Gabriel PASCUAL[1], Júlia SOLIVA[1], Jordi MAZON[1,2], David PINO[2,3]

[1]*Escola d'Enginyeria en Telecomunicacions i Aeroespacial de Castelldefels, Universitat Politècnica de Catalunya, 08860 Castelldefels (Barcelona), Spain.*

[2]*Department of Physics, Universitat Politècnica de Catalunya, 08034 Barcelona, Spain.*

[3]*Institut d'Estudis Espacials de Catalunya, 08860 Castelldefels (Barcelona), Spain.*

ABSTRACT

Turbulence represents a primary hazard for aviation, with Clear-Air Turbulence (CAT) posing a unique threat due to its visually undetectable nature. This study evaluates the 75-year temporal evolution of the macro-environmental atmospheric conditions favorable to CAT over Europe and North Africa from 1950 to 2025. Using monthly ERA5 reanalysis data at 200 and 225 hPa, seven synoptic-scale diagnostic indices were analyzed: Horizontal Divergence (HDG), Richardson Number (Ri), NCSU1, Brown Index (BRI), Ellrod Index (EI1, EI2), and Potential Vorticity (PV). Results demonstrate that while domain-averaged indicators such as NCSU1, BRI, PV, and EI1 show a long-term increase in the frequency of CAT-prone environments, others, including HDG and EI2, exhibit no clear trend. In contrast, the Richardson Number displays a statistically significant decreasing trend, reflecting a shift toward reduced atmospheric stability and enhanced shear at these upper-tropospheric levels. Furthermore, spectral analysis via Fast Fourier Transform identifies a dominant periodicity of 2.45 years in the HDG and PV indices. This cycle aligns with historical findings of quasi-biennial solar activity, suggesting that the large-scale background conditions driving regional CAT potential

*Corresponding author: Jordi MAZON
Email: jordi.mazon@upc.edu

over Europe may be modulated by solar-driven stratospheric dynamics. These findings underscore the index-dependent nature of regional synoptic trends and the importance of distinguishing macroscopic climate precursors from microscale turbulence events in aviation safety risk assessments.

Key words: Clear-air turbulence; ERA5 reanalysis; Synoptic-scale dynamics; Upper troposphere; Quasi-biennial solar modulation; Euro-Mediterranean region.

Running title: 75-year climatology of Large-Scale Atmospheric Conditions Favorable to CAT

Acknowledgments. The authors acknowledge the use of the ERA5 reanalysis data generated by the European Centre for Medium-Range Weather Forecasts (ECMWF) and accessed via the Copernicus Climate Change Service (C3S) Climate Data Store.

Funding. There is not funding

Conflict of Interest statement: Authors have not any conflict of interest.

Permission to reproduce material from other sources. Not applicable

Data availability statement. Not applicable

1. Introduction

Since the beginning of commercial aviation, atmospheric turbulence has remained a primary concern for stakeholders due to its implications for aeronautical safety and passenger comfort. Defined as abrupt and stochastic fluctuations in vertical air velocity, turbulence represents a significant operational hazard. While various typologies exist,

including mechanical, convective, and orographic, Clear-Air Turbulence (CAT) is particularly critical. CAT occurs in the upper troposphere and lower stratosphere, typically associated with intense wind shear in cloud-free regions. Its lack of visual or radar signatures renders it undetectable to flight crews, significantly increasing the risk of structural damage or injuries to occupants (WMO, 2025).

International standards, as established by the International Civil Aviation Organization (ICAO), utilize the Eddy Dissipation Rate (EDR) as the universal metric for quantifying CAT intensity (Bechtold et al., 2021). Despite its relevance, the accurate modeling of turbulence remains one of the most complex challenges in fluid dynamics, primarily due to the non-linear nature of the governing equations and the high computational cost required for high-resolution atmospheric simulations.

The possible intensification of Clear Air Turbulence (CAT) has emerged as one of the most significant challenges for commercial aviation in the 21st century. William (2016) discusses the increased fuel consumption and structural wear caused by navigating more turbulent airspaces. During the last two decades, several authors have investigated whether a warming atmosphere leads to an intensification of CAT. William and Joshi (2013) were pioneers in quantifying the relationship between CAT and CO_2 concentrations. Using climate models, these authors demonstrated that doubling CO_2 concentrations in the atmosphere could lead to a 40% to 170% increase in the frequency of moderate-to-severe CAT in the North Atlantic during winter. This study shifted the discourse from viewing CAT as a static meteorological hazard to a dynamic variable influenced by anthropogenic climate change.

Williams (2017) focused on transatlantic flights from UK and North America, highlighting that the increase in CAT is not uniform across all seasons. The winter months show the most significant intensification due to the stronger temperature gradients between the Arctic and the mid-latitudes. Storer et al. (2017) provided a global perspective, confirming that the atmospheric conditions conducive to CAT (measured via various diagnostics like the Ellrod Index) are becoming more frequent across most of the Northern Hemisphere. These authors conducted climate model simulations finding that by 2050–2080, climate change will cause large relative increases in CAT globally, with the volume of severe turbulence approximately doubling over Europe, North America, and the North Pacific. These shifts are particularly pronounced at midlatitudes, where future severe CAT may become as frequent as moderate CAT was historically. The findings underscore a critical need for improved operational forecasting and flight planning to mitigate rising risks to aviation safety and comfort.

To provide a robust dynamical basis for CAT augmentation projections, De Medeiros et al. (2025) show that anthropogenic warming strengthens vertical wind shear at 250 hPa by 27% while decreasing atmospheric stratification and the Richardson number by 47%. These findings suggest that future atmospheric conditions will become increasingly favorable for the generation of clear-air turbulence, particularly under high-emission scenarios. This evolution poses a direct and escalating challenge to aviation safety and the efficiency of global flight operations in a warming climate.

Jaeger et al. (2007) studied a 44-year ERA40 climatology (1958–2001), identifying a 40 to 90% increase in CAT indicators over the North Atlantic, the US, and Europe. These authors found winter maxima over major coastal and mountainous regions, with frequencies

closely tied to jet stream positioning. Their findings emphasize that while most CAT indices are jet-dependent, hydrostatic instability remains predominantly land-based and seasonally distinct. Additionally, Prosser et al. (2023) analyzed atmospheric trends between 1979 and 2020, revealing that average annual exposure to severe CAT at specific coordinates across the North Atlantic grew by 55%, increasing from 17.7 hours at the start of the study period to 27.4 hours by 2020. Lee et al. (2019) explored the impact of vertical shear on aviation flight levels within European airspace. They found that the increase in shear at the tropopause level is significantly outpacing the increase in average wind speeds, suggesting that the atmosphere is becoming more "unstable" even if the jet stream position remains relatively constant.

Based on 41 years of ERA5 data (1979–2019), Lee et al. (2023) identified critical CAT hotspots over East Asia, the Eastern Pacific, and the Northwestern Atlantic, primarily driven by strong vertical wind shear and jet stream dynamics. Long-term increasing trends in turbulence potential are observed in these regions, with the most significant intensification occurring over East Asia due to a strengthening jet stream and heightened meridional temperature gradients. These changes are attributed to a complex thermal pattern of tropical warming and Eurasian cooling, posing substantial challenges for future aviation efficiency across the Pacific and Atlantic corridors. Since 2000 pilot reports have transitioned toward Automated Turbulence Reporting and high-resolution reanalysis data like ERA5. Sharman and Pearson (2017) discuss the integration of these automated systems into forecasting models, noting that while the ability to predict the "location" has improved, the "intensity" remains difficult to calibrate due to the multi-scale nature of turbulence.

Lee et al. (2025) used ERA5 data and in situ measurements to identify nearly 5,000 turbulence events, linking them to specific synoptic features like Rossby wave breaking and warm conveyor belts. They found that 40% of events that are driven by high horizontal deformation within Rossby wave breaking regions, while another 30% are associated with warm conveyor belt ascent and negative potential vorticity. These authors provide a physical framework for understanding CAT triggers, emphasizing that ERA5 is a robust dataset for studying CAT.

The goal of the present study is to provide a comprehensive spatio-temporal climatological analysis of the large-scale atmospheric environments favorable to CAT over the Euro-Mediterranean region (75ºN to 20ºN; 35ºW to 50ºE) spanning a 75-year period (1950–2025). By utilizing monthly ERA5 reanalysis data, this investigation shifts the focus toward the long-term variability of synoptic-scale CAT precursors rather than microscale turbulence events, which cannot be captured at this temporal resolution. The analysis targets the 200 hPa and 225 hPa pressure levels. While CAT exhibits significant vertical sensitivity (e.g., Storer et al., 2017), these pressure levels typically coincide with the mid-latitude jet stream core and the oscillating boundary of the tropopause, where macroscopic vertical wind shear and static stability gradients are most pronounced (e.g., Jaeger and Sprenger, 2007). Furthermore, from an aeronautical engineering perspective, these levels represent the standard optimal cruise altitudes for long-haul commercial aviation. Therefore, analyzing the evolution of these macro-environmental turbulence risk zones at these specific heights provides direct, climate-scale insights into operational safety, fuel efficiency, and structural load impacts in a changing climate (Williams, 2017).

Using monthly averaged data to analyze phenomena that occur on timescales of seconds or minutes, such as Clear-Air Turbulence (CAT), is a well-established paradigm in climate dynamics. This macroscopic approach mirrors methodologies widely used in the study of other highly localized, transient atmospheric events, such as severe convective storms and deep convective outbreaks. In those fields, researchers do not track individual, short-lived convective cells; instead, they utilize monthly or seasonal averages of reanalysis data to assess large-scale thermodynamic proxies, such as Convective Available Potential Energy (CAPE) or vertical wind shear, to map the shifting boundaries of storm-prone environments (e.g., Brooks et al., 2003; Diffenbaugh et al., 2013).

Applying this logic to aviation hazards, calculating diagnostic indices from monthly ERA5 fields acts as a temporal low-pass filter. While this filtering removes the stochastic noise of individual turbulence encounters, it effectively uncovers the steady, low-frequency variability of the background flow. By shifting the analytical lens from the transient micro-event to the macro-environmental envelope, monthly data provide a robust framework for identifying multi-decadal trends and teleconnection modulations. This allows researchers to determine whether the "atmospheric climate" is becoming systematically more or less conducive to generating the sharp shear zones and structural instabilities that ultimately trigger microscale aviation risks.

This paper is structured as follows: Section 2 establishes the methodology including the mathematical definitions of the seven CAT indices used; Section 3 details the results obtained; Section 4 discusses the main findings; and finally, Section 5 summarizes the primary conclusions.

2. Methodology

Variables to analyze CAT at cruise levels from 1950 to 2025 were obtained from ERA5 reanalysis at the Climate Data Store (CDS) (Hersbach et al., 2018), a cornerstone of the Copernicus Climate Change Service (C3S). Operated by the European Centre for Medium-Range Weather Forecasts (ECMWF) on behalf of the European Commission, the C3S provides open-access, high-fidelity climate variables designed to support European Union mitigation and adaptation policies (Hersbach et al., 2023). The dataset is structured on a regular latitude-longitude grid with a high horizontal resolution of 0.25° x 0.25°. To accurately capture Clear-Air Turbulence (CAT) dynamics at commercial aviation altitudes, the following specifications were applied:

- Vertical Coverage: Data spans 37 pressure levels, ranging from 1000 hPa to 1 hPa. This study specifically extracts variables at the 200 and 225 hPa levels, corresponding to standard cruise altitudes.
- Temporal Resolution: Monthly averages were utilized to identify long-term climatic trends rather than transient weather events.
- Variable Selection: To compute the indices, from the sixteen distinct atmospheric variables available, the following ones were necessary: geopotential, potential vorticity (PV), the three components of the wind velocity (u, v, w), temperature (T), and relative vorticity.

We analyzed CAT at the two pressure levels from 1950 to 2025 in the geographical area limited at 75 º N and 20 º N in latitude and at 50 º E and 35 º W in longitude (see Figure 1).

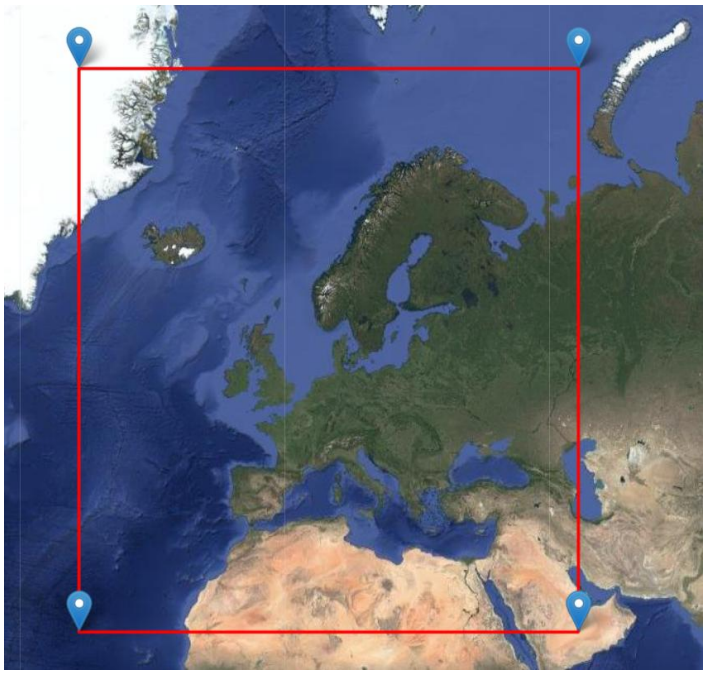


Figure 1. Geographical area of the study (source Google Earth).

2.1 Definition of the analyzed indices to describe CAT

From the 21 indices proposed by Prosser et al. (2023), seven have been selected for this study based on their consistency in existing literature (e.g. Prosser et al., 2023; Sharman et al., 2006; William et al., 2013) and their ability to provide a multifaceted perspective of atmospheric turbulence.

- Horizontal Divergence (HDG). It is the net outflow of air from an air parcel in the horizontal direction. Divergence is the sum of two components, directional divergence, and speed divergence. Directional divergence occurs when air escapes the air parcel in several directions but at a constant wind speed. On the other hand, Speed divergence occurs when, within the same isobaric surface, wind speed increases with height. The mathematical definition is:

$$HDG = \frac{du}{dx} + \frac{dv}{dy} \qquad (1)$$

The intensity of vertical motion in the atmosphere is directly related to these processes: stronger vertical motions are associated with greater divergence or convergence.

- Negative Richardson Number (Ri). The Richardson Number represents the dimensionless ratio of buoyancy to shear generation, serving as a fundamental measure of atmospheric stability (Sharman et al., 2006). In this study, the sign convention is inverted (negative Ri) to ensure that higher index values correspond to higher turbulence potential, aligning the metric with standard eddy dissipation rates indicators:

$$\mathrm{Ri} = -\frac{N^2}{S_v} = -\frac{\left(\frac{g \cdot B}{\theta}\right)^2}{S_v} \qquad (2)$$

Where g is gravitational acceleration, θ is potential temperature, and S_v is the modulus of gradient of horizontal wind speed in the vertical direction:

$$S_v = \sqrt{\left(\frac{\partial u}{\partial z}\right)^2 + \left(\frac{\partial v}{\partial z}\right)^2} \qquad (3)$$

Values near 0 of *Ri* indicate mechanical turbulence, while positive values exceeding 0.03 suggest predominant convective motion (SKYbrary Aviation Safety, 2024).

- Brown Index (BRI). It is a simplification of the Richardson number tendency equation. It utilizes the thermal wind relation to approximate horizontal wind gradients, offering a theoretical assessment of turbulence intensity (Sharman et al., 2006):

$$\mathrm{BRI} = \frac{1}{24} \cdot \Phi \cdot S_v^2 \qquad (4)$$

where:

$$\Phi = \sqrt{0.3 \cdot \zeta_a^2 + DSH^2 + DST^2},$$

and:

$$\mathrm{DST} = \frac{\partial u}{\partial x} - \frac{\partial v}{\partial y},$$

$$\mathrm{DSH} = \frac{\partial u}{\partial y} - \frac{\partial v}{\partial x}$$

are the stretching and shearing components of the deformation. Additionally, ζ_a represents absolute vorticity ($\zeta_a = \zeta_r + f$, where ζ_r is relative vorticity and f is the Coriolis frequency).

- North Carolina State University Index (NCSU1). Developed to characterize pre-turbulent conditions associated with severe aviation hazards, the NCSU1 integrates localized rotation, vertical wind shear, and buoyancy-related instability (Sharman et al., 2006):

$$\mathrm{NCSU1} = \frac{1}{MAX(Ri, 10^{-5})} \cdot MAX\left(u \cdot \frac{\partial u}{\partial x} + v \cdot \frac{\partial v}{\partial y}, 0\right) \cdot |\nabla \zeta_r| \qquad (5)$$

This index identifies the flow's capacity to amplify minor perturbations into significant turbulent energy, particularly in regions influenced by the jet stream or orographic features (Kaplan et al., 2003).

- Potential Vorticity (PV). It is defined as the absolute circulation of an air parcel between isentropic surfaces. It is a critical tracer for identifying the tropopause and small-scale structures often overlooked by geopotential height analysis (RAMMB/CIRA, s.f.):

$$\mathrm{PV} = -g \cdot \zeta_a \cdot \frac{\partial \theta}{\partial p} \qquad (6)$$

where p is the pressure. Although useful for identifying atmospheric boundaries, its efficacy in quantifying mesoscale CAT remains a subject of comparative analysis (Storer et al., 2017).

- Ellrod Indices *(*EI1 and EI2*).* Ellrod and Knapp (1992) developed this index on the premise that deformation (DEF) and vertical wind shear (VWS) are the primary kinematic precursors to CAT. The basic version (EI1) is defined as:

$$\mathrm{EI1} = \mathrm{VWS} \cdot \mathrm{DEF} \qquad (7)$$

where:

$$\mathrm{VWS} = \frac{\sqrt{\Delta u^2 + \Delta v^2}}{\Delta z}$$

and

$$\mathrm{DEF} = \sqrt{DST^2 + DSH^2}$$

A second variant (EI2) incorporates horizontal divergence, which can significantly contribute to turbulence in specific synoptic environments:

$$\mathrm{EI2} = \mathrm{VWS}(\mathrm{DEF} - \mathrm{HDG}) \qquad (8)$$

Verification against Pilot Reports (PIREPs) has demonstrated that using EI2 as an indicator for CAT presents probability of detection (POD) between 70% and 84%, confirming its practical utility for aviation forecasting (Ellrod et al., 1992).

2.2 Numerical Discretization and Computational Procedure

To characterize the spatio-temporal evolution of CAT over Europe, the processed diagnostic fields are analyzed by considering temporal and spatial averaging. Regarding temporal averaging, annual and seasonal mean fields are calculated across the spatial domain. For the final year of the series (2025), the average is truncated at August due to data availability. Seasonal averages are partitioned into meteorological quarters (e.g., Winter: DJF; Spring: MAM), noting that the 1950 winter season is omitted because it requires December 1949 data.

To analyze the evolution of the calculated indices during the studied period, they were averaged over the entire domain to produce a single representative value per time step (monthly, seasonal, or annual). Finally, to evaluate the inter-index relationships and

identify periodicities within the 76-year time series, two primary mathematical frameworks are employed: non-parametric correlation and frequency-domain decomposition.

Given that a preliminary visual inspection of the data suggests a non-Gaussian distribution, the Spearman rank correlation coefficient (ρ) is utilized rather than Pearson's linear correlation. This method transforms the absolute index values into ordinal ranks (from 1 to 76), thereby assessing the monotonic relationship between variables while mitigating the influence of outliers. The resulting coefficients range from -1 (perfect inverse correlation) to +1 (perfect direct correlation). To ensure the robustness of these associations, the Student's t-test is applied to derive p-values. A threshold of $p<0.05$ is established to define statistical significance, ensuring that observed correlations are not the result of stochastic variability.

The second statistical analysis aims to detect cyclical patterns that may be obscured by high-frequency noise in the time domain, such as the solar cycle. The Fast Fourier Transform (FFT) is applied to the annually averaged series to analyze the potential solar cycle influence on CAT frequency. The FFT serves as an efficient algorithm to compute the Discrete Fourier Transform (DFT), decomposing the temporal signal into its constituent frequency components (Raikar et al., 2024). For analytical clarity, these frequencies are converted into annual periods. The significance of periodic peaks is determined by analyzing their spectral amplitude. Isolated peaks with high relative amplitude suggest deterministic physical forcing, whereas multiple peaks of similar magnitude may indicate a non-periodic or random signal. In cases where the dominant amplitude corresponds to a period exceeding the observational window, the secondary peak is prioritized for physical interpretation.

3. Results

3.1 Correlation Analysis of CAT Indices

The Spearman's Correlation test is used to determine the correlation between the different turbulent indices (see Table 1 for 200 hPa and Table 2 for 225 hPa).

Table 1. Spearman's correlation test results between the turbulent indices at 200 hPa. The upper side of the matrix represents the degree of correlation and the lower side of the *p*-value of the correlation. In bold the largest (smallest) values of the correlation (*p*-value).

200 hPa	EI1	EI2	HDG	Ri	NCSU1	PV	BRI
EI1		**0.841**	0.098	-0.082	**0.787**	-0.394	**0.771**
EI2	**$2.17\cdot10^{-21}$**		-0.395	-0.218	0.593	-0.208	0.585
HDG	0.398	$4.07\cdot10^{-4}$		0.140	-0.023	0.103	-0.001
Ri	0.482	0.059	0.226		0.026	-0.015	-0.078
NCSU1	**$3.75\cdot10^{-17}$**	$1.69\cdot10^{-8}$	0.843	0.826		-0.363	0.499
PV	$4.36\cdot10^{-4}$	0.071	0.376	0.895	$1.27\cdot10^{-3}$		-0.439
BRI	**$3.97\cdot10^{-16}$**	$2.78\cdot10^{-8}$	0.997	0.502	$4.55\cdot10^{-6}$	$7.37\cdot10^{-5}$	

Table 2. Same as Table 1 at 225 hPa.

225 hPa	EI1	EI2	HDG	Ri	NCSU1	PV	BRI
EI1		**0.825**	-0.109	-0.181	**0.798**	-0.446	**0.705**
EI2	**$4.75\cdot10^{-20}$**		-0.418	-0.319	0.588	-0.134	0.452
HDG	0.347	$1.75\cdot10^{-4}$		0.171	-0.036	0.004	0.071
Ri	0.117	$4.95\cdot10^{-3}$	0.139		-0.164	-0.143	0.003
NCSU1	**$6.35\cdot10^{-18}$**	$2.39\cdot10^{-8}$	0.756	0.156		-0.399	0.457
PV	$5.40\cdot10^{-5}$	0.247	0.969	0.218	$3.45\cdot10^{-4}$		-0.441
BRI	**$1.19\cdot10^{-12}$**	$4.24\cdot10^{-5}$	0.543	0.981	$3.38\cdot10^{-5}$	$6.68\cdot10^{-5}$	

The statistical evaluation of inter-index relationships reveals that the Ellrod Index 1 (EI1) serves as the most robust proxy for general turbulence trends within the study domain. As detailed in Tables 1 and 2, EI1 exhibits a highly significant correlation (ρ>0.70) with three primary indices: EI2, the North Carolina State University Index (NCSU1), and the Brown Index (BRI).

The most pronounced association was observed between EI1 and EI2. This result is consistent with their shared theoretical origin (Ellrod and Knapp, 1992); both indices utilize vertical wind shear (VWS) and deformation (DEF) as fundamental kinematic precursors. The difference in their correlation (ρ<1.0) is attributable to the inclusion of the horizontal convergence term (-HDG) in EI2, which enhances diagnostic accuracy in specific synoptic environments (see Equations 2.20 and 2.21).

Furthermore, the strong correlation between EI1 and NCSU1 stems from their mutual dependence on VWS. Similarly, the relationship between EI1 and BRI is driven by the treatment of the deformation tensor; while BRI explicitly incorporates the shearing (DSH) and stretching (DST) components, EI1 utilizes the total deformation magnitude. Additionally, both indices are linked through the inclusion of the wind shear modulus (S_v).

All reported correlations reached statistical significance with *p*-values consistently below the α=0.05 threshold. However, the strength of these relationships exhibited sensitivity to pressure levels:

- Upper Level (200 hPa): EI2 and BRI demonstrated higher correlation coefficients with EI1, suggesting that deformation-based turbulence is more consistent at higher altitudes.
- Lower Level (225 hPa): The correlation between EI1 and NCSU1 peaked at this level, potentially reflecting the influence of jet stream dynamics near the lower boundary of the cruise altitude.

Conversely, EI1 showed negligible correlation (ρ<0.10) with both Horizontal Divergence (HDG) and the Richardson Number (Ri). A moderate negative correlation was identified with Potential Vorticity (PV), particularly at 225 hPa, likely reflecting the inverse relationship between PV-defined stability and turbulent kinetic energy.

Indices that correlate strongly with EI1 also exhibit significant associations with EI2. This inter-dependency is expected given that EI2 is a functional variant of EI1. The relative decrease in correlation between NCSU1/BRI and EI2, compared to their relation with EI1, is explained by the presence of the convergence term in EI2, which is absent in the former indices. This hypothesis is supported by the moderate negative correlation found between EI2 and HDG; since HDG represents the mathematical opposite of convergence, its influence is uniquely captured by EI2.

Finally, a moderate correlation was observed between NCSU1 and BRI, once again mediated by the vertical wind shear modulus. Potential Vorticity exhibited a consistent moderate negative correlation across the deformation-based index suite (EI1, NCSU1, and BRI).

3.2 *Temporal evolution of the indices*

The temporal evolution at annual and seasonal averaged indices over the domain of HDG, NCSU1 and Ri has been analyzed. Similarities and differences between the indices, as well as the trends, are studied, providing a robust basis to determine if CAT has increased or not over time.

There are several reasons to choose these indices. First NCSU1 is chosen because it represents the influence of orographic features, and specifically mountain waves that are directly related with the generation of CAT. Then, Ri is chosen because it was the first index that was developed to forecast CAT in the 1960s, other indices such as BRI have been developed using Ri as basis furthermore EI1 and EI2 were developed in order to improve the results provided by Ri, finally NCSU1 also incorporates Ri in one of the terms of its definition but its influence may not be present. Consequently, even not being the most accurate index is the basis of the prediction of CAT and has been widely used with 3.6 million results in Google Scholar. Also, most of the indices focus on vertical motions such as VWS or pressure variations, HDG focuses only on horizontal motions. No other indices were used to obtain temporal evolutions due to lack of time. The linear regression function was applied to the seven considered indices to determine which of them present significant changes in the evolution of CAT over the studied period.

3.2.1 Annual evolution

The first parameter subjected to individual assessment is Horizontal Divergence (HDG), prioritized due to its exceptionally low correlation with other turbulent diagnostics. This suggests that HDG captures distinct atmospheric processes not represented by deformation-based indices. As illustrated in Figure 2 (upper panels), the temporal evolution of the domain-averaged HDG at 200 hPa exhibits a slope coefficient of $8.82 \cdot 10^{-10}$ $s^{-1}yr^{-1}$, which is approximately three orders of magnitude smaller than the mean HDG values recorded throughout the study period. A linear regression significance test yielded a *p*-value of 0.532, which significantly exceeds the standard α=0.05

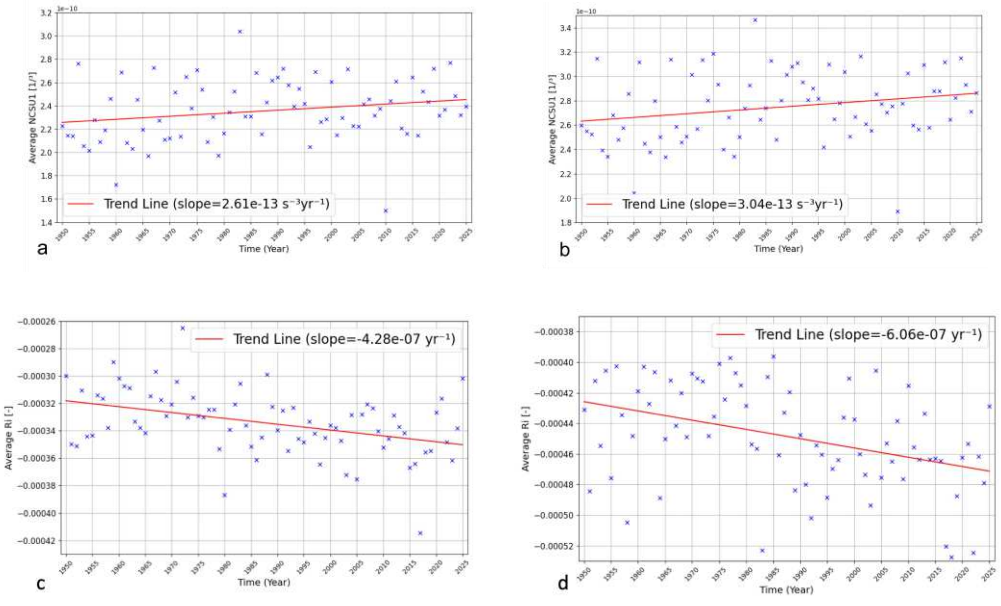
threshold. Consequently, the null hypothesis, which posits no linear trend, cannot be rejected, confirming the absence of a statistically significant increase in horizontal divergence over the analyzed period.

A similar pattern is observed at the 225 hPa pressure level (Figure 2b), where the linear regression yields a slope of $1.36 \cdot 10^{-9}$ $s^{-3} \cdot yr^{-1}$. Coupled with a coefficient of determination (R^2) of 0.01 and a p-value of 0.358, these results reinforce the lack of a discernible long-term trend at lower cruise altitudes. A comparative analysis reveals a highly correlated distribution between the two levels, with net annual values remaining positive, indicating a structural predominance of divergence within the domain. The primary distinction is a consistent vertical offset, with HDG values at 225 hPa typically ranging from $0.1 \cdot 10^{-6}$ $s^{-1}yr^{-1}$ to $0.3 \cdot 10^{-6}$ $s^{-1}yr^{-1}$ lower than those at 200 hPa.

Complementing this analysis, the Negative Richardson Number (Ri) was examined as a primary indicator of atmospheric stability. Like HDG, Ri demonstrates a low correlation with the remaining indices. The middle panels of Figure 2 (c and d) represent the temporal evolution of the averaged Ri at 200 hPa and 225 hPa, respectively. At 200 hPa, the linear regression identifies a negative slope of $-4.28 \cdot 10^{-7}$ yr^{-1}. Despite a low R^2 of 0.16, which is indicative of substantial interannual variability, the resulting p-value of $2.88 \cdot 10^{-4}$ yr^{-1}confirms a statistically significant negative trend. Physically, the negative values recorded throughout the series correspond to atmospheric conditions dominated by mechanical turbulence. However, the observed downward trajectory indicates that Ri values are progressively decreasing. According to the theoretical framework, as values approach the -0.1 threshold, the atmosphere trends toward stable stratification,

paradoxically suggesting a shift toward a less turbulent environment at these specific pressure levels.

Finally, the North Carolina State University Index (NCSU1) was analyzed, which, in contrast to the previous metrics, correlates well with the broader suite of deformation-based indices. The lower panels of Figure 2 (e and f) detail the annual evolution of NCSU1, where the index reached a maximum of $3 \cdot 10^{-10}$ s^{-3} in 1983 and a minimum of $1.52 \cdot 10^{-10}$ s^{-3} in 2010. The trend line reveals a positive slope of $2.61 \cdot 10^{-13}$ s^{-3} yr^{-1}. Notably, the *p*-value is precisely 0.05, indicating a statistically significant increase. However, the low R^2 of 0.05 emphasizes that the signal is characterized by significant interannual variability, which must be considered when interpreting long-term intensification.



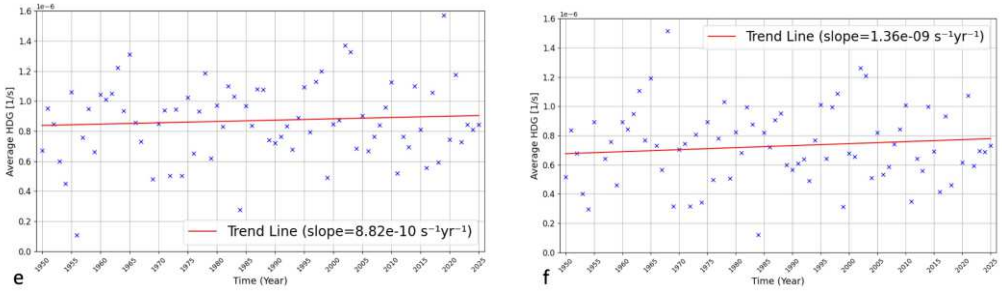


Figure 2. Temporal evolution of the annual averages over the domain of HDG (top panels) at a) 200 hPa and b) 225 hPa, Ri (middle panels) at c) 200 hPa and d) 225 hPa , North Carolina State University Index (bottom panels) at e) 200 hPa and f) 225 hPa. The red lines show the linear trend.

3.2.2 Seasonal evolution

Figure 3 shows the seasonal temporal evolution of HDG at 200 hPa. As with the annual evolution, the main differences between 200 hPa and 225 hPa (not shown) are the previously mentioned offsets. Compared to the annual evolution, a major difference is observable: for all seasons except spring, negative HDG values occurred for many years. Additionally, for winter, the HDG trend is negative. This suggests that winters have become more stable, potentially due to rising temperatures affecting lapse rates.

It can also be observed that dispersion is much smaller in the seasonal evolution than in the annual evolution, indicating low seasonal variability. Spring presents the smallest variability, with all values indicating divergence. Autumn likewise exhibits very low variability but presents some negative values representing convergence. Summer is the most stable season, with most of the values falling between $0.5 \cdot 10^{-6}$ s^{-1} and 0. Finally

winter exhibits much greater interannual spread than the other seasons; specifically, 74 out of the 75 winters present divergence, while 1956 and 2018 present convergence. As in the annual evolution, the conclusion is that there is no evidence of a significant increase in HDG during the studied period.

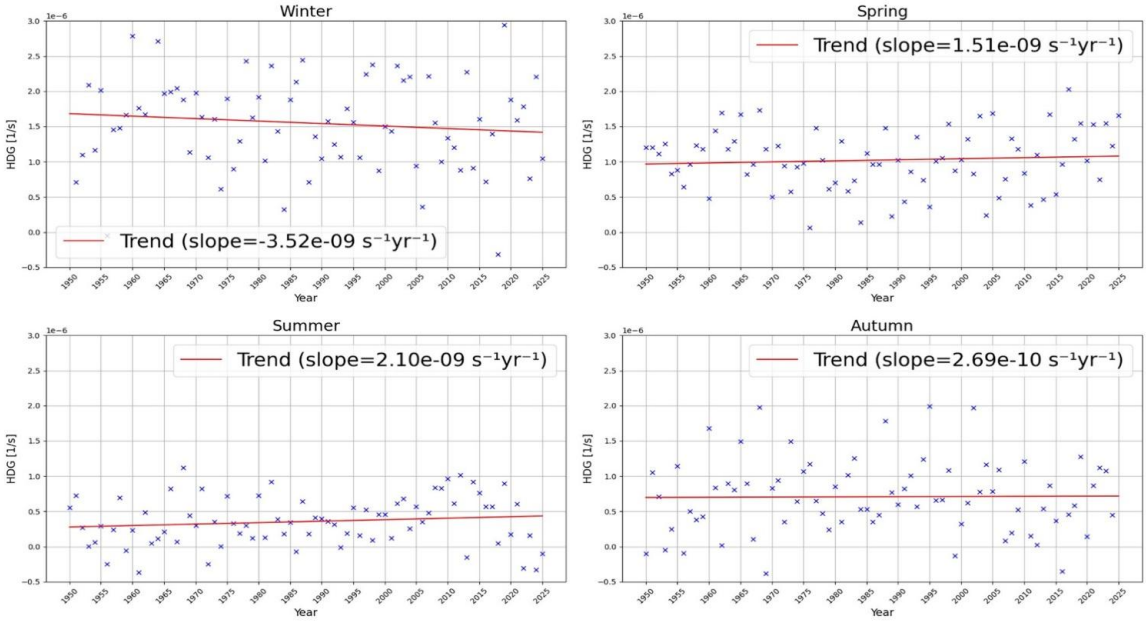


Figure 3. Temporal evolution of the seasonal average over the domain of HDG at 200 hPa. The red line shows the lineal trend.

Figure 4 presents the seasonal evolution for the averaged Ri over the domain at 200 hPa is presented. The evolution at 225 hPa is very similar. Beginning with winter, only a slight decreasing trend in the occurrence of CAT is found. The winter values are the closest to 0 compared to both the other seasons and the annual evolution, implying that this is the season in which the strongest mechanical turbulence is present. This result also indicates that winter is the most turbulent season. The interannual variability is slightly

greater than that of the annual evolution. For spring, the most noticeable difference compared to the other seasons and the annual evolution is that the trend line has a positive slope. This indicates that for this season throughout the studied period, an increase in the occurrence of CAT is found. Additionally, the values are higher than those for the annual evolution, showing greater interannual variability is shown compared to both the winter and annual trends.

Summer and autumn present similarities in the evolution of the index. In summer, the strongest trend is observed as the slope of the trend line is the steepest compared to the other seasons. Notably, between 1966 and 1977 (with the exception of 1969), a continuous descending trend is distinguishable. Most of the values are higher than those present in the annual trends, indicating that summers are more stable than the annual averages. The interannual variability is similar to that observed in the winter graph.

The last season of the year, autumn, likewise presents a negative trend, albeit one that is more attenuated than in summer as can be seen by comparing the slopes. It presents low interannual variability and the values are the lowest of all the four seasons indicating that it is the most stable one. These values are also lower than the annual averaged values.

Summarizing, three out of four seasons present a negative trend similar to the annual evolution; in contrast, spring presents a positive trend with a very high interannual variability.

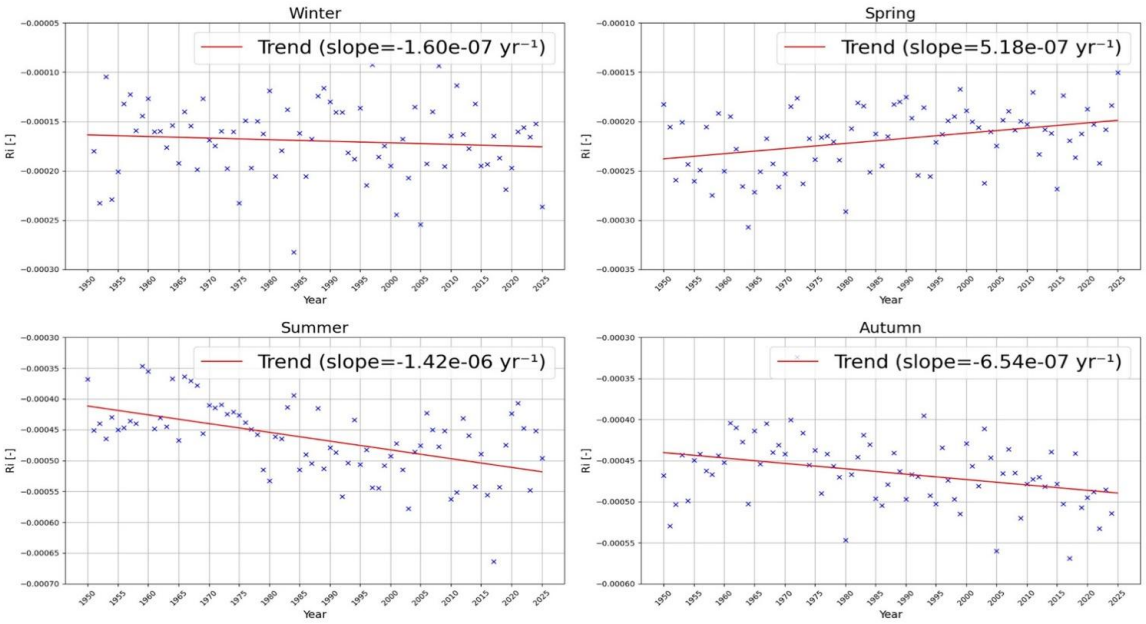


Figure 4. Same as Figure 3 for the negative Richardson number.

Figure 5 shows the temporal evolution of the average NCSU1 values over the domain for each season. As with the other indices, only the 200 hPa plots are shown; same as HDG, the 225 hPa data only exhibits an offset compared to the 200 hPa plots.

Winter presents the highest values of all four seasons, indicating that it is the most turbulent period. In some cases, the values are twice as large as those recorded in the annual evolution. Regarding the trend line, the slope is slightly steeper than for the annual trend and is the steepest among all seasons. The interannual variability is also the highest during this period.

In spring, the values are slightly lower than in winter but slightly higher than in summer and autumn. The slope of the trend line is smaller than in winter. A study of the interannual variability reveals a change in behavior starting in 1995: prior to this year, most of the values were close to the trend line and each other; however, since 1995, values have become much more dispersed.

Summer and autumn present more similarities to each other than the aforementioned two seasons. In summer, the values are slightly lower than in the annual evolution and lower than in winter and spring. Remarkably, the trend line slope in summer is five orders of magnitude smaller than the values of the variable itself, indicating that no appreciable evolution is present. However, it can be observed that from 1960 to 1970 most of the values fall below the trend line, from 1970 to 1990, they are above the line and from 1990 to the end of the period they are again below the line.

Autumn presents a behavior very similar to summer. The values are very comparable, and the trend line presents an almost insignificant slope. In this case, the near-zero slope does not represent any clear evolution. The major difference from summer is that the interannual variability is greater, and the previously described cyclical pattern is not visible.

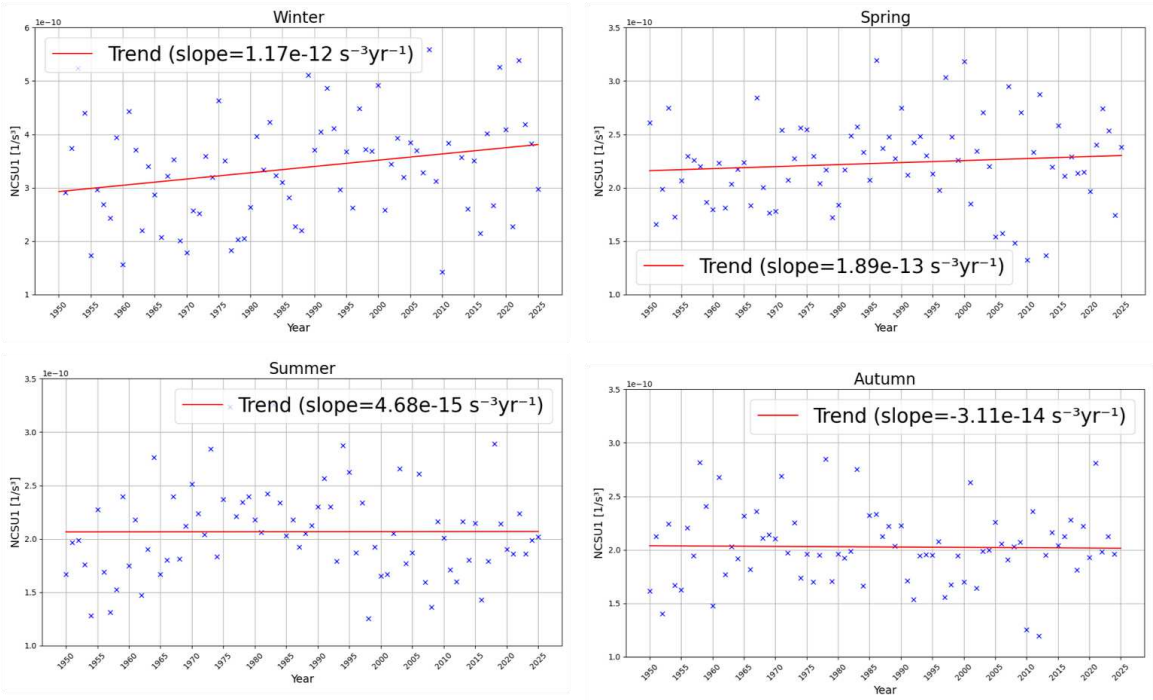


Figure 5. Same as Figure 4 for the NCSU1.

Table 3 and 4 detail the slope of the trend line, the R^2 and the p-value for the three turbulent indices at 200 hPa and 225 hPa, respectively. Regarding the seasonal analysis, it is observed that winter is the most turbulent season. For HDG and NCSU1, winter presents the greatest variations and the most significant increases over the period, while for Ri, the opposite is observed. In contrast, during the summer, HDG and NCSU1 present fewer variations, while for Ri this is the season where the greatest decreasing trend in turbulence is observed.

Table 3. Linear regression results for NCSU1, Ri and HDG at 200 hPa in the period 1950-2025.

200 hPa	**Slope**	**R^2**	***p*-value**
NCSU1	$2.61 \cdot 10^{-13}\ s^{-3} \cdot yr^{-1}$	0.041	0.057
Ri	$-4.28 \cdot 10^{-7}\ yr^{-1}$	0.164	$2.88 \cdot 10^{-4}$
HDG	$8.82 \cdot 10^{-10}\ s^{-1} \cdot yr^{-1}$	$5.29 \cdot 10^{-3}$	0.532

Table 4. Linear regression results for NCSU1, Ri and HDG at 225 hPa in the period 1950-2025.

225 hPa	**Slope**	**R^2**	***p*-value**
NCSU1	$3.04 \cdot 10^{-13}\ s^{-3} \cdot yr^{-1}$	0.055	0.041
Ri	$-6.06 \cdot 10^{-7}\ yr^{-1}$	0.162	$3.17 \cdot 10^{-4}$
HDG	$1.36 \cdot 10^{-9}\ s^{-1} \cdot yr^{-1}$	0.011	0.358

3.3 FFT Analysis

Figure 6 shows the FFT analysis applied to the temporal evolution of the domain-averaged HDG. The dominant period is identified at 2.45 years (f=0.4 yr^{-1}). Historical research by Clough (1928), which demonstrated that when the influence of the 11-year solar cycles is eliminated, variations in solar activity with shorter periods become observable, with the most common period being approximately 2.4 years. It was further argued that this periodicity was not accidental; if the observed variations were stochastic, 1.6 years would be the most probable interval rather than the observed 2.4 years. Furthermore, the years in which this shortest-term period occurs do not necessarily coincide with the onset of a new 11-year solar cycle.

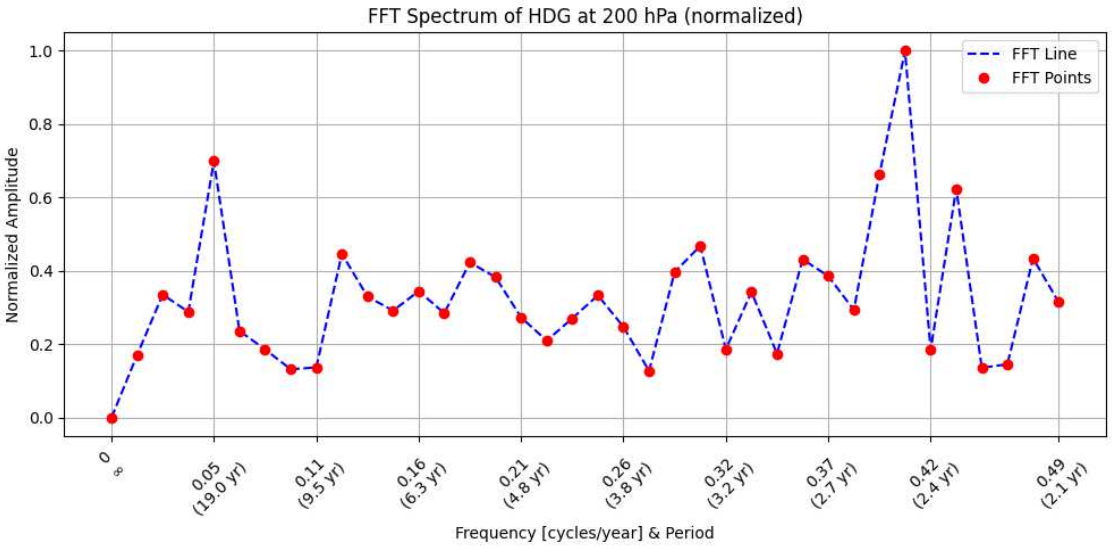
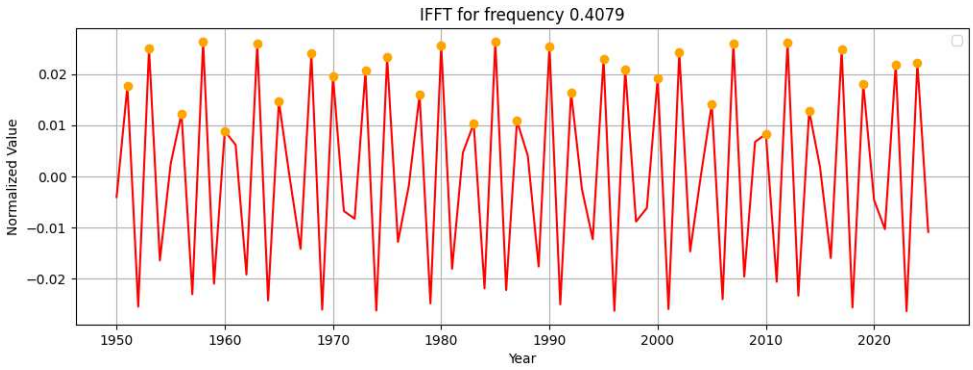


Figure 6. FFT analysis for HDG index

Figure 7 shows the Inverse Fast Fourier Transform (IFFT) specifically performed for the 2.45-year period. Through this computation, it is possible to identify the specific years in which this phenomenon occurred; however, to isolate these fluctuations, the long-term trend must first be removed. As can be seen, the difference between the normalized peak

543 and troguh values is approximately 0.015. Given that the HDG values have an order of
544 magnitude of 10^{-6}, a resultant difference of $1.5 \cdot 10^{-8}$ difference in HDG units is obtained,
545 meaning that all reconstructed values are nearly identical in magnitude.
546 Comparing the years marking the onset of solar cycles from 1950 to 2025 (e.g. Clough,
547 1928) with the years in which the 2.45-year periodicities are most prominent, none of
548 them coincide. Consequently, these fluctuations may indeed be related to the previously
549 mentioned 2.4-year solar cycles rather than the primary 11-year cycle.

550
551



552
553 Figure 7. IFFT for the 2.45-year period.
554
555 Similar spectral analyses were performed for the remaining indices. Table 5 details the
556 frequencies associated with the highest relative amplitudes in the FFT spectrum for all
557 seven turbulent indices at both pressure levels.

558

559 Table 5. Results for the FFT most relevant frequencies for the turbulent indices (in yr^{-1}).
560 In bold, frequencies corresponding to the short-period solar cycles.

	Frequency at 200 hPa ***(yr^{-1})***	**Frequency at 225 hPa** ***(yr^{-1})***
NCSU1	0.3553	0.3553
Ri	0.1711	0.3158

HDG	**0.4079**	**0.4079**
EI1	0.1316	0.1316
EI2	0.1316	0.3553
BRI	0.2500	0.1974
PV	**0.4211**	**0.4211**

4. Discussion: comparative analysis

Our results for Europe exhibit several key differences from previous studies focused on the North Atlantic. While Prosser et al. (2023) identified a 55% surge in severe CAT over the North Atlantic, trends across the European continent exhibit greater index-dependency, particularly within the HDG framework. This regional consistency suggests that the atmospheric intensification observed in transatlantic corridors, driven by the widening temperature gradient at the tropopause, is less uniform over landmasses. Unlike the open ocean, where the jet stream experiences uninterrupted strengthening, the atmospheric profile over continental Europe is influenced by complex orographic forcing and higher surface roughness. These factors can disrupt the coherence of vertical wind shear, leading to a more localized and stable HDG index compared to the streamlined, shear-dominant maritime flight tracks.

In the context of the PV-based diagnostic framework, the observed significant decreasing trend in Potential Vorticity directly translates to an intensified turbulence signal, providing a robust empirical contrast to the more cautious projections reported by Storer et al. (2017). While those authors utilized climate models to project future CAT responses, their findings often exhibited lower confidence levels regarding historical PV-

583 related trends due to the inherent smoothing and coarse resolution of global climate
584 simulations. In contrast, the ERA5 reanalysis captures the historical signal with greater
585 acuity by assimilating vast arrays of observational data into a high-resolution grid. This
586 allows for a more precise reconstruction of the vertical stability and vorticity gradients
587 that define Potential Vorticity. Consequently, the use of ERA5 identifies a definitive
588 historical decline in PV, and a corresponding rise in turbulence, that may be
589 underrepresented in the broader, multi-model ensembles used in previous climate impact
590 studies.
591 Regarding solar influence, several authors have investigated the quasi-biennial period in
592 various atmospheric phenomena. Qiang et al. (2007) used the Empirical Mode
593 Decomposition (EMD) method to process nonlinear and non-stationary sunspots
594 sequences, effectively identifying isolated features across various scales. Analysis of
595 sunspot data reveals periodic components of 1.3-1.4 years, 25-30 months (QBO), and 11-
596 year and 22-year cycles. The 11-year solar cycle emerges as the most dominant
597 component, exhibiting the highest amplitude and correlation with original sunspot
598 numbers, though a period of around 2.5 years was also identified. Khramova et al. (2002)
599 found quasi-biennial oscillations of solar activity using Singular Spectrum Analysis to
600 separate out and analyze these oscillations. The principal components of the solar cycle
601 are stable 11-year, secular, and quasi-biennial variations. The periods and shapes of
602 individual variations in each quasi-biennial train depend on the length and power of the
603 particular 11-year cycle.
604 Vokhmyanin et al. (2023) found that sudden stratospheric warmings (SSWs),
605 characterized by a breakdown of the polar vortex and significant surface weather impacts,

606 are strongly influenced by the interplay between solar/geomagnetic activity and the
607 Quasi-Biennial Oscillation (QBO). By modeling these relationships, the authors achieved
608 an 86% success rate in predicting winter SSW occurrences as early as the preceding
609 August. The observed 2.45-year CAT period is coherent with previous studies linking
610 solar activity to CAT intensity. In particular, the 2.45-year periodicity observed in CAT
611 intensity demonstrates a high degree of coherence with solar variations, mediated by the
612 QBO and its influence on the Northern Hemisphere winter.
613 Furthermore, Camp et al. (2007) analyzed sunspot data, utilizing methods like Empirical
614 Mode Decomposition and Singular Spectrum Analysis, to isolate stable quasi-biennial
615 cycles (roughly 2.4 to 2.5 years) that mirror this CAT periodicity. This connection is
616 physically grounded in the interplay between solar maxima and QBO phases.
617 Specifically, the easterly phase (eQBO) interacts with solar activity to precondition the
618 polar vortex for sudden stratospheric warmings (SSWs). When these SSWs occur, they
619 trigger a dramatic breakdown of the polar vortex, which in turn disrupts the jet stream,
620 the primary driver for enhanced CAT across Europe. By modeling this synergy between
621 geomagnetic activity and the QBO, researchers such as Vokhmyanin et al. (2023) have
622 achieved an 86% success rate in predicting winter SSW occurrences as early as the
623 preceding August. This high predictability underscores that the 2.45-year CAT cycle is
624 not a random fluctuation; rather, it is a direct atmospheric reflection of how solar-driven
625 oscillations modulate the large-scale stratospheric dynamics that dictate turbulent
626 conditions in the upper troposphere.
627

628 **5. Conclusions**

The objective of this work was to analyze whether the macro-environmental background conditions favorable to CAT have changed over the Euro-Mediterranean region during the last 75 years (1950–2025). While previous literature has demonstrated that transient CAT events have increased due to climate change over North America and the North Atlantic regions, this research specifically focused on the long-term temporal evolution of the synoptic-scale atmospheric precursors over Europe. By utilizing monthly ERA5 reanalysis data, this macroscopic approach effectively filters out the high-frequency stochastic noise of individual, minute-scale turbulence events to uncover multi-decadal structural shifts in the upper-tropospheric circulation. To do so, seven different indices related to turbulence dynamics were evaluated (HDG, Ri, NCSU1, EI1, EI2, PV, BRI). Prior to addressing the main climatological trends, it was necessary to assess the cross-correlations between these diagnostic tools when applied to time-averaged fields. Using the Spearman's Correlation function on annually averaged values, remarkable similarities were found among EI1, EI2, NCSU1, and BRI, while HDG, PV, and Ri did not show a clear relationship to the other indices. Based on these results, HDG, Ri, and NCSU1 were selected for the subsequent trend analysis to provide a broader, non-redundant perspective on the changing behavior of the large-scale flow. To answer the primary research question, the temporal evolution of the annual averages for the three selected indices was analyzed. All indicators exhibited significant interannual variability, and the resulting multi-decadal trends varied across the indices, underscoring the index-dependent nature of regional climate projections. Linear regression revealed a statistically significant positive trend in the NCSU1, suggesting a long-term expansion of atmospheric configurations prone to

652 generating CAT. Concurrently, the Richardson Number (Ri) showed a statistically
653 significant decreasing trend, indicating a systematic shift toward reduced static stability
654 and enhanced macroscopic vertical wind shear, which aligns with the NCSU1 results. In
655 contrast, the HDG index did not exhibit a clear annual trend. Given the pronounced
656 interannual variability, the seasonal evolution of these macro-environmental indices was
657 also examined. This seasonal analysis indicates that the winter background environment is
658 the most conducive to triggering CAT instabilities, while summer conditions tend to be the
659 most quiescent. For all three indices, the temporal evolution during the summer and autumn
660 months presented greater structural similarities to each other than to winter and spring.
661 Regionally, the seasonal trends also diverged: for HDG, all seasons except winter showed
662 an increasing trend in line with the annual pattern. For Ri, all seasons except spring
663 displayed a descending trend, consistent with a year-round shift toward a more unstable
664 upper-tropospheric background flow. Finally, the NCSU1 winter, spring, and annual trends
665 demonstrated an increase in turbulence potential, whereas summer showed almost no trend
666 and autumn exhibited a slightly decreasing propensity. Overall, these results demonstrate
667 that while microscale turbulence cannot be directly resolved at monthly resolutions, long-
668 term reanalysis averages successfully track the shifting climatological envelope of aviation
669 safety risks.

670 Finally, the possible effect of solar cycles on the index values was studied using FFT
671 analysis. None of the indices showed a periodicity corresponding to the 11-year solar cycle.
672 However, HDG and PV exhibited a potential relationship with the 2.4-year solar cycle
673 analyzed by Clough (1928). While it is not yet possible to definitively establish a causal
674 link, the observed periodicities align with the quasi-biennial solar variations described in

675 historical literature. Although contemporary references specifically confirming this short-
676 period cycle are limited, the hypothesis that the periodicities observed in HDG and PV are
677 modulated by short-period solar cycles is remains tentatively supported and requires further
678 validation using longer time series or higher-resolution solar proxy data.
679

680

681 **REFERENCES**
682

683 Bechtold, P., Beljaars, A., Bozzo, A., Buizza, R., Carlson, E., Fielding, M., Giovannini,
684 F., Haiden, T., Hogan, R. J., Leutbecher, M., Maidl, M., Magnusson, L., Roberts, C., &
685 Vitart, F., 2021: Forecasting clear-air turbulence. *ECMWF Newsletter*, (168), 18–26.
686 https://www.ecmwf.int/en/newsletter/168/meteorology/forecasting-clear-air-turbulence
687

688 Brooks, H. E., Lee, J. W., & Craven, J. P. (2003). The spatial and temporal distribution of
689 severe thunderstorms and tornadoes. *Atmospheric Research*, 67-68, 73–94.
690

691 Camp, C. D., and K. Tung, 2007: The Influence of the Solar Cycle and QBO on the Late-
692 Winter Stratospheric Polar Vortex. *J. Atmos. Sci.*, **64**, 1267–1283,
693 https://doi.org/10.1175/JAS3883.1.
694

695 Clough, H. W., 1928: The 28-month period in solar activity and corresponding periods in
696 magnetic and meteorological data. *Mon. Wea. Rev.*, **56**, 251–264,
697 https://doi.org/10.1175/1520-0493(1928)56<251:TMPISA>2.0.CO;2.

De Medeiros, J., Williams, P.D., 2025: Future Trends in Upper-Atmospheric Shear Instability from Climate Change. *J. Atmos. Sci.*, **82**, 2375–2392, https://doi.org/10.1175/JAS-D-24-0283.1.

Diffenbaugh, N. S., Scherer, M., & Trapp, R. J. (2013). Robust increases in severe thunderstorm environments in response to greenhouse forcing. *Proceedings of the National Academy of Sciences*, 110(41), 16361–16366. https://doi.org/10.1073/pnas.1307758110

Ellrod, G. P., Knapp, D. I., 1992: An objective method for forecasting clear-air turbulence based on the product of relative intensity and vertical wind shear. *Weather and Forecasting*, 7(1), 150–165. https://doi.org/10.1175/1520-0434(1992)007<0150:AOCATF>2.0.CO;2

Hersbach, H., Bell, B., Berrisford, P., Biavati, G., Horányi, A., Muñoz Sabater, J., Nicolas, J., Peubey, C., Radu, R., Rozum, I., Schepers, D., Simmons, A., Soci, C., Dee, D., Thépaut, J-N., 2023: ERA5 hourly data on single levels from 1940 to present. Copernicus Climate Change Service (C3S) Climate Data Store (CDS), DOI: 10.24381/cds.adbb2d47 (Accessed on 20-02-2026)

719 Hersbach, H., Bell, B., Berrisford, P., Hirahara, S., Horányi, A., Muñoz-Sabater, J.,
720 Nicolas, J., Peubey, C., Radu, R., Schepers, D., Simmons, A., Soci, C., Abdalla, S.,
721 Abellan, X., Balsamo, G., Bechtold, P., Biavati, G., Bidlot, J., Bonavita, M., … Thépaut,
722 J-N., 2018: *ERA5 hourly data on pressure levels from 1950 to present*. Copernicus
723 Climate Change Service (C3S) Climate Data Store (CDS).
724 https://doi.org/10.24381/cds.bd0915c6

725 Jaeger, E. B., Sprenger, M., 2007: A Northern Hemispheric climatology of indices for
726 clear air turbulence in the tropopause region derived from ERA40 reanalysis data. *J.*
727 *Geophys. Res.*, **112**, D20106, https://doi.org/10.1029/2006JD008189.

728 Kaplan, M. L., Lin, Y.-L., 2003: *Characterizing the preturbulence environment for*
729 *sensor development, new hazard algorithms and NASA experimental flight planning*
730 (NAG-1-02007). North Carolina State University. NASA Technical Reports Server.
731 https://ntrs.nasa.gov/api/citations/20040110976/downloads/20040110976.pdf
732

733 Khramova, M.N., Kononovich, E.V. & Krasotkin, S.A., 2002: Quasi-Biennial
734 Oscillations of Global Solar-Activity Indices. *Solar System Research* **36**, 507–512.
735 https://doi.org/10.1023/A:1022161304847
736

737 Lee, S. H., Williams, P. D., Niconeeva, T. H., 2019: Evidence for sharp increase in North
738 Atlantic jet stream vertical wind shear. Nature, 572(7771), 639-642.
739 https://doi.org/10.1038/s41586-019-1465-z
740

741 Lee, M. H. F. and Sprenger, M., 2025: Clear-air turbulence derived from in situ aircraft
742 observation – a weather feature-based typology using ERA5 reanalysis, Weather Clim.
743 Dynam., 6, 1583–1604, https://doi.org/10.5194/wcd-6-1583-2025

744 Lee, J. H., Kim, J.-H., Sharman, R. D., Kim, J., Son, S.-W., 2023: Climatology of clear-
745 air turbulence in upper troposphere and lower stratosphere in the Northern Hemisphere
746 using ERA5 reanalysis data. *J. Geophys. Res. Atmos.*, **128**, e2022JD037679,
747 https://doi.org/10.1029/2022JD037679.

748 Prosser, M. C., Williams, P. D., Marlton, G. J., & Harrison, R. G., 2023: Evidence for
749 large increases in clear-air turbulence over the past four decades. Geophysical Research
750 Letters, 50(11), e2023GL103814. https://doi.org/10.1029/2023GL103814
751

752 RAMMB/CIRA. (s.f.). *Numerical parameters for synoptic- to mesoscale cloud systems:*
753 *Potential Vorticity*. WMO Virtual Laboratory; EUMETSAT.
754 https://rammb.cira.colostate.edu/wmovl/vrl/tutorials/satmanu-
755 eumetsat/satmanu/basic/parameters/pv.htm
756

757 Raikar, G., Pai, S., 2024: *Fast Fourier transform (FFT): Concept, advantages,*
758 *applications, & facts*. Encyclopedia Britannica. https://www.britannica.com/science/Fast-
759 Fourier-transform
760

761 SKYbrary Aviation Safety., 2024: *Richardson number*.
762 https://skybrary.aero/articles/richardson-number

Sharman, R. D., Pearson, J.M., 2017: Prediction of energy dissipation rates for aviation turbulence. Part I: Forecasting nonconvective turbulence. *Journal of Applied Meteorology and Climatology* 56.2: 317-337. https://doi.org/10.1175/JAMC-D-16-0205.1

Sharman, R., Tebaldi, C., Wiener, G., & Wolff, J., 2006: An integrated approach to mid- and upper-level turbulence forecasting. *Weather and Forecasting*, *21*(3), 268–287. https://doi.org/10.1175/WAF924.1

Storer, L. N., Williams, P. D., Joshi, M. M., 2017: Global response of clear-air turbulence to climate change. Geophysical Research Letters, 44(19), 9976-9984. https://doi.org/10.1002/2017GL074618

Vokhmyanin, M., Asikainen, T., Salminen, A., & Mursula, K., 2023: Long-term prediction of sudden stratospheric warmings with geomagnetic and solar activity. *Journal of Geophysical Research: Atmospheres*, 128, e2022JD037337. https://doi.org/10.1029/2022JD037337

Williams, P.D., 2017: Increased light, moderate, and severe clear-air turbulence in response to climate change. *Adv. Atmos. Sci.* **34**, 576–586. https://doi.org/10.1007/s00376-017-6268-2

786 Williams, P. D., Joshi, M. M., 2013: Intensification of winter transatlantic aviation
787 turbulence in response to climate change. Nature Climate Change, 3(7), 644-648.
788 https://doi.org/10.1038/nclimate1866
789
790 Williams, P.D., 2016: Transatlantic flight times and climate change. Environmental
791 Research Letters, 11 (2). 024008. ISSN 1748-9326 doi: 10.1088/1748-9326/11/2/024008
792